

TCSA-UDA: Text-Driven Cross-Semantic Alignment for Unsupervised Domain Adaptation in Medical Image Segmentation

Lalit Maurya, Honghai Liu, and Reyer Zwiggelaar

Abstract—Unsupervised domain adaptation (UDA) for medical image segmentation remains a significant challenge due to substantial domain shifts across imaging modalities, such as CT and MRI. While recent vision-language representation learning methods have shown promise, their potential in UDA segmentation tasks remains underexplored. To address this gap, we propose TCSA-UDA, a Text-driven Cross-Semantic Alignment framework that leverages domain-invariant textual class descriptions to guide visual representation learning. Our approach introduces a vision–language covariance cosine loss to directly align image encoder features with inter-class textual semantic relations, encouraging semantically meaningful and modality-invariant feature representations. Additionally, we incorporate a prototype alignment module that aligns class-wise pixel-level feature distributions across domains using high-level semantic prototypes. This mitigates residual category-level discrepancies and enhances cross-modal consistency. Extensive experiments on challenging cross-modality cardiac, abdominal and brain tumor segmentation benchmarks demonstrate that our TCSA-UDA framework significantly reduces domain shift and consistently outperforms state-of-the-art UDA methods, establishing a new paradigm for integrating language-driven semantics into domain-adaptive medical image analysis. The code is available at https://github.com/lalitmaurya47/TCSA_UDA

Index Terms—Unsupervised domain adaptation, cross-semantic alignment, cross modality learning, vision-language model, medical image segmentation,

I. INTRODUCTION

Medical image segmentation employs modalities like CT and MRI to offer detailed anatomical insights for diagnosis and surgical planning. While CT provides high spatial resolution and bone detail, MRI excels in soft tissue contrast [1]. Although clinicians can intuitively integrate multi-modal data, models trained on a single modality often fail to generalize across domains due to differences in imaging protocols, scanners, and institutions. Fully-supervised deep learning methods perform well in-domain but are sensitive to domain shifts, which are common in real-world medical data. Annotating data from each new domain is labor-intensive and often impractical in clinical workflows. Moreover, domain variability in medical imaging, stemming from acquisition settings and equipment differences, poses a significant challenge to model robustness [2]. Thus, there is a critical need for domain-adaptive models

Lalit Maurya and Honghai Liu are with the School of Computing, University of Portsmouth, Portsmouth, PO1 3HE, UK (e-mail: lalit.maurya@port.ac.uk ; honghai.liu@port.ac.uk).

Reyer Zwiggelaar is with the Department of Computer Science, Aberystwyth University, Aberystwyth, SY23 3DB, UK (e-mail: rrz@aber.ac.uk).

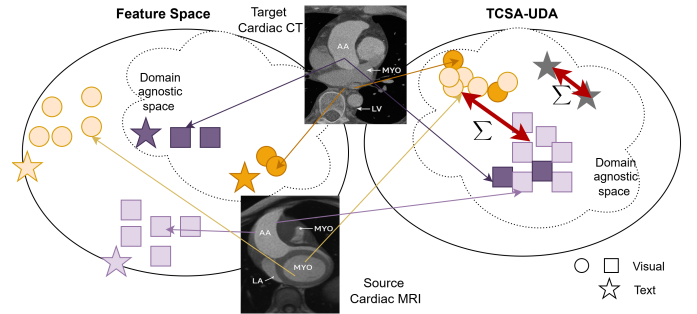


Fig. 1. Class-specific visual features (squares and circles) from source and target domains are aligned with domain-agnostic text embeddings (stars) via covariance matching. Red bidirectional arrows represent cross-modal covariance learning, encouraging semantic consistency across domains in a shared feature space

capable of generalizing across diverse data distributions without relying on extensive re-annotation, ensuring reliable and scalable deployment in clinical environments. Recently, Unsupervised Domain Adaptation (UDA) in computer vision has gained momentum due to its ability to transfer knowledge from labeled source domains to unlabeled target domains, effectively reducing reliance on manual annotation [3], [4]. In particular, image-level approaches focus on appearance adaptation using image-to-image translation [5], while feature-level methods aim to learn domain-invariant representations [6]. Many UDA methods employ adversarial training or distance-based metrics like maximum mean discrepancy (MMD) [7] to align distributions across domains [8], [9]. Some strategies also perform adaptation in the output space to align the spatial structure of predictions [6], [10]. However, these often rely on cross-entropy loss, which may lead to overconfident and miscalibrated predictions in the target domain, particularly due to the absence of target supervision. Self-training under a teacher–student framework has been explored as an alternative, where pseudo-labels from a teacher model guide the student model. Yet, self-training is highly sensitive to label noise, and standard data augmentation techniques often fail to capture the complex variations in medical imaging domains [11], [12].

Critically, current UDA pipelines lack robust semantic consistency across domains. We posit that modality-aware semantic guidance is a missing element. Unlike visual features, textual class descriptions (e.g. “left atrium”, “tumor”) offer domain-invariant semantics, yet their expression can vary with imaging modality (e.g. MRI vs. CT). Building on this insight,

we propose incorporating text-embeddings to guide visual representation learning via cross-modal covariance learning with adversarial training (Fig. 1). This encourages domain- and modality-aligned feature spaces, enhancing intra-class compactness and inter-class separability, even in the absence of target supervision. The contribution of our work is listed below:

- We introduce a text-driven cross-semantic alignment paradigm for UDA in medical image segmentation that integrates vision–language covariance cosine loss to directly align image encoder features with textual semantic relations for improved segmentation.
- We design a transformer-based fusion module to integrate vision features with modality-specific text embeddings, allowing the model to leverage context-aware semantic cues tailored to each imaging modality.
- We integrate a semantic prototype alignment strategy that enforces class-wise feature consistency between source and target domains, addressing residual distribution shifts and enhancing cross-modal consistency.
- Demonstrate the effectiveness of the proposed method in reducing domain shift and improving segmentation performance on challenging cross modality cardiac structure, abdominal organ and brain tumor segmentation.

II. RELATED WORK

Unsupervised Domain Adaptation. UDA techniques aim to minimize performance discrepancies between source and target domains caused by domain shifts. These techniques can be categorized into image-level adaptation, feature-level adaptation, and output-level adaptation. Image-level methods such as CycleGAN [5] transform source images to mimic the target domain, improving segmentation training. Feature-level approaches utilize adversarial learning to extract domain-invariant features [7], [13]. Output-level strategies focus on aligning spatial layouts and semantic structures [14], [15]. Recent advancements incorporate more adaptive strategies. SECASA [6] introduces entropy-guided constraints and semantic alignment, while DPCL [16] leverages evolving class prototypes and contrastive learning to enhance discriminative representation. Additionally, Transformer-based architectures such as DAFormer [17] and MA-UDA [18] demonstrate improved generalization by integrating hierarchical attention mechanisms and meta-adaptation for cross-modality segmentation. Deng et al. [2] proposed an unsupervised electron microscopy (EM) image denoising method using domain alignment and adversarial training to disentangle content and noise. However, most existing approaches are limited to visual modalities and fail to utilize semantic cues embedded in language. The integration of multimodal information, particularly from vision-language models, presents a promising but underexplored direction for enhancing domain adaptation in medical image segmentation.

Text-Assisted Medical Image Segmentation. Recent advances in medical image segmentation have demonstrated the effectiveness of integrating textual and visual information to boost performance. TGANet [19] leveraged text embeddings

for colonoscopy segmentation, surpassing image-only methods. Zhong et al. [20] showed that language-guided segmentation improves Dice scores while reducing data demands. Liu et al. [21] introduced frozen language models to stabilize training and enrich latent representations. Chen et al. [22] extended vision-language pretraining to 3D imaging using synthetic text annotations to address data scarcity. However, most approaches remain limited to single-modality inputs and rely solely on text embeddings, which fail to fully mitigate domain shift effects. To address this, our method incorporates a vision–language covariance cosine loss to directly align image encoder features with inter-class textual semantics, fostering modality-invariant and semantically meaningful feature representations that enhance cross-domain generalization in medical segmentation tasks.

III. METHODOLOGY

A. Problem Definition and Overall Framework

A key challenge in UDA is the domain shift between the labeled source domain I^{src} and the unlabeled target domain I^{trg} , which leads to poor generalization of models trained only on I^{src} . To address this, UDA methods aim to learn domain-invariant representations by jointly leveraging both domains during training. This can be mathematically formulated as [23]:

$$\mathcal{F}_{\text{UDA}} : I^{\text{src}} \cup I^{\text{trg}} \rightarrow Y^{\text{src}} \cup Y^{\text{trg}} \quad (1)$$

where, \mathcal{F}_{UDA} is a mapping function learned using the labeled source domain $\mathcal{D}_S : \{I^{\text{src}}, Y^{\text{src}}\}_{i=1}^{N_s}$ and the unlabeled target domain $\mathcal{D}_T : \{I^{\text{trg}}\}_{i=1}^{N_t}$. Here, each (i th) source and target image $I_i^{\text{src}}, I_i^{\text{trg}} \in \mathbb{R}^{1 \times H \times W}$ and the correspondence label $Y_i^{\text{trg}} \in \{1, \dots, C\}^{H \times W}$. Here, C represent the classes and $H \times W$ denotes the size of image. In adversarial learning [14], a segmentation network G generates predictions, and a discriminator D attempts to distinguish whether these predictions originate from the source or target domain. The network G is trained to deceive D generating target-like predictions. Although adversarial approaches are effective, conventional UDA frameworks typically assume domain homogeneity [24]. In real-world medical scenarios, datasets often span multiple imaging modalities such as CT, MRI, and ultrasound across both source and target domains. These modalities are often unpaired and heterogeneous, and can be denoted as $\{D_{M_1}, D_{M_2}, \dots, D_{M_N}\}$.

We therefore extend UDA to a cross modal adaptation setting, aiming to train a single segmentation model capable of generalizing across diverse modalities. To facilitate this, we incorporate text embeddings $T \in \mathbb{R}^d$, derived from class labels or clinical descriptions medical descriptions using pretrained language models (e.g. CLIP [25] or BioGPT [26]). These embeddings guide the visual feature learning via cross-attention or projection alignment, providing semantic priors that improve consistency across both domains and modalities. The problem is thus formulated as learning a unified function $G(I, T)$ that jointly minimizes domain discrepancy and enhances cross-modal semantic alignment without requiring target labels.

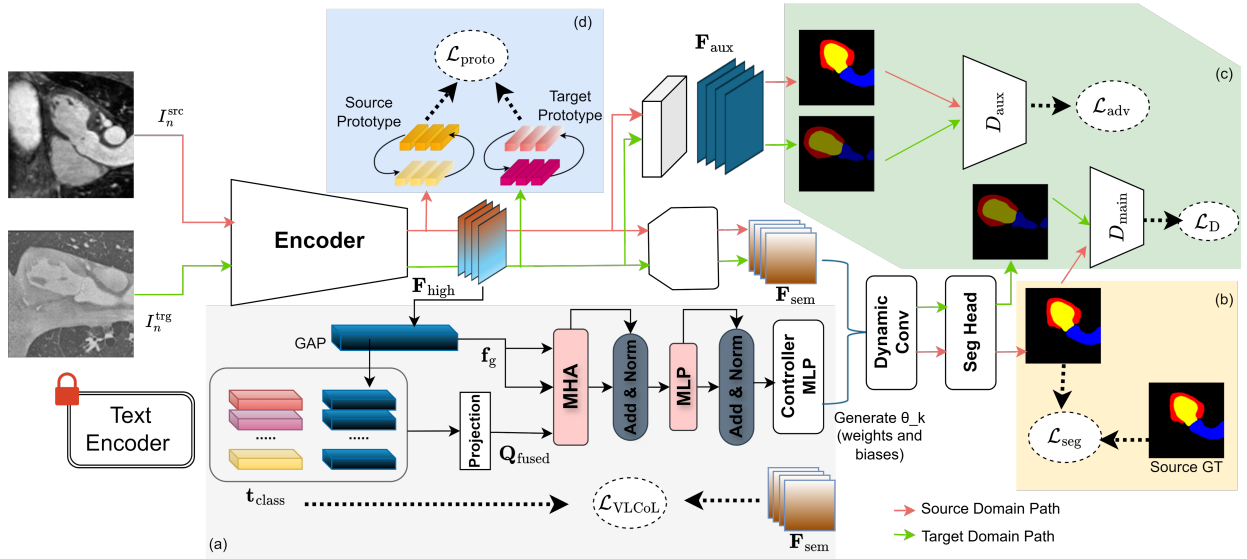


Fig. 2. Schematic representation of the proposed TCSA-UDA framework, comprising: (a) text-driven semantic covariance learning via \mathcal{L}_{VLCoL} , (b) text-driven supervised learning on the source domain via \mathcal{L}_{seg} , (c) adversarial learning using both text-driven and auxiliary predictions via \mathcal{L}_{adv} , and (d) class-wise cross-domain semantic alignment via \mathcal{L}_{proto} .

The overall architecture of our proposed approach is illustrated in Fig. 2 and consists of three key components. First (Fig. 2 (a) and (b)), to address cross-domain medical image segmentation, we propose a modality-aware vision-language fusion framework that integrates modality-specific text embeddings with visual features using a transformer-based fusion module guided by dynamic convolution. This design enables effective generalization across imaging modalities such as CT and MRI, without requiring pixel-level annotations from the target domain. Second (Fig. 2 (c)), we employ two Generative Adversarial Networks (GANs) to perform domain alignment through adversarial learning. The generator produces two outputs: (i) a text-driven segmentation prediction used for supervised learning on the source domain, and (ii) an auxiliary prediction that generates self-information maps for both source and target domains, used to fool domain discriminators (D_{main} and D_{aux}). This adversarial setup encourages domain-invariant predictions and category-aware adaptation. Third (Fig. 2 (d)), to mitigate residual class-level distribution mismatches that are not fully addressed by entropy-based constraints, we incorporate an adaptive prototype alignment module. This module leverages class-level feature representations and aligns them across domains, facilitating consistent pixel-level feature alignment of corresponding semantic categories between the source and target domains. The detailed implementation of each component is described in the following subsections.

B. Text-Driven Cross Domain Learning

Text-driven cross domain learning helps the model perform well on different imaging types like CT and MRI. As shown in Fig. 2, our encoder architecture builds on DeepLabV2 with a ResNet backbone to extract multi-scale features. A parallel text branch provides modality-specific semantic guidance, and a transformer-based fusion module aligns the visual and textual features for better cross-domain understanding. The encoder

outputs high-level features $\mathbf{F}_{high} \in \mathbb{R}^{B \times 2048 \times H \times W}$. These features undergo a sequence of convolutions with channel dimensions [1024, 512, 256, 128] to refine visual representations, resulting in semantic feature $\mathbf{F}_{sem} \in \mathbb{R}^{B \times 256 \times H \times W}$. The classifier uses atrous (dilated) convolutions to capture multi-scale context, produces auxiliary segmentation logits $\mathbf{F}_{aux} \in \mathbb{R}^{B \times C \times H \times W}$, where B is batch size, $H \times W$ are features spatial dimensions, and C is the number of classes. Semantic text embeddings are generated using modality-specific medical prompts for each organ/class. This embedding is produced by a pretrained medical language model such as CLIP, or BioBERT [26] using a descriptive prompt formatted as a template “A {Dataset} {CT/MRI} imaging of a [CLS]”. Here, {CT/MRI} specifies the imaging modality, either computed tomography or magnetic resonance, {Dataset} represents specific medical dataset type such as cardiac or abdominal, and [CLS] is replaced with a class-specific anatomical term (e.g. myocardium of the left ventricle, left atrium blood cavity). This results in class-level semantic embeddings specific to each modality. For a given input image, the embedding corresponding to its modality $\mathbf{E}_{modality}$, is selected and projected to a 256-dimensional space to produce $\mathbf{t}_{class} \in \mathbb{R}^{C \times 256}$, which captures semantic encoding for each class.

On the vision side, high-level global features \mathbf{F}_{high} are aggregated using global average pooling, followed by group normalization and a 1×1 convolution to produce $\mathbf{F}_{GAP} \in \mathbb{R}^{B \times 256 \times 1 \times 1}$. The output is then flattened to form a global visual feature vector $\mathbf{f}_g \in \mathbb{R}^{B \times 1 \times 256}$. This global feature is repeated C times to match the number of classes, resulting in $\mathbf{f}_{rep} \in \mathbb{R}^{B \times C \times 256}$, so that it can be concatenated with the corresponding \mathbf{t}_{class} . The concatenated semantic and visual features are passed through a linear layer with ReLU to obtain the fused query representation $\mathbf{Q}_{fused} \in \mathbb{R}^{B \times C \times 256}$. This fused query is used in a multi-head attention (MHA) module, where \mathbf{f}_g is used as both the key and value. This

allows class-specific text embeddings to attend selectively to informative visual features. A multi-layer perceptron (MLP) refines this fused representation, enabling precise modality-aware semantic segmentation.

$$\mathbf{F}_{\text{fused}} = \text{MLP}(\text{MHA}(\mathbf{Q}_{\text{fused}}, \mathbf{f}_g, \mathbf{f}_g)) \in \mathbb{R}^{B \times C \times 256} \quad (2)$$

From the fused features, we predict convolution parameters dynamically using an MLP controller:

$$\theta_k = \text{MLP}(\text{mean}(\mathbf{F}_{\text{fused}}, \text{dim} = 1)) \in \mathbb{R}^{B \times (256 \times 128 + 128)} \quad (3)$$

This parameters generates dynamic convolution weights $\mathbf{W} \in \mathbb{R}^{B \times 128 \times 256 \times 1 \times 1}$ and biases $\mathbf{b} \in \mathbb{R}^{B \times 128}$ for each input sample. This mechanism allows per-sample convolution filter generation, improving model adaptability to modality-specific features. For each visual sample \mathbf{F}_{sem} a customized convolution is applied

$$\mathbf{f}^{\text{conv}} = \text{Conv2D}(\mathbf{F}_{\text{sem}}, \mathbf{W}, \mathbf{b}) \in \mathbb{R}^{B \times 128 \times H \times W} \quad (4)$$

This dynamic filtering enables flexible and context-sensitive processing, crucial for fine-grained segmentation across diverse imaging types. A final Seg Head is applied to produce the segmentation mask. For a source labeled mask $\mathbf{Y}_n^{\text{src}}$, the segmentation loss \mathcal{L}_{seg} is calculated as

$$\mathcal{L}_{\text{seg}} = \sum_{n=1}^N (\mathcal{L}_{\text{CE}}(P_n^{\text{src}}, \mathbf{Y}_n^{\text{src}}) + \mathcal{L}_{\text{Dice}}(P_n^{\text{src}}, \mathbf{Y}_n^{\text{src}})) \quad (5)$$

where, P_n^{src} is the source image prediction of proposed segmentation model. \mathcal{L}_{CE} and $\mathcal{L}_{\text{Dice}}$ denote the cross-entropy and Dice loss functions.

C. Vision-Language Covariance Cosine Loss (VLCoL)

VLCoL enforces that the relationships (covariances) among class-specific pixel features extracted from the segmentation encoder match the relationships among corresponding text embeddings of those classes. The alignment is done by minimizing the cosine distance between the two covariance matrices. This encourages the segmentation encoder’s latent space to reflect the semantic structure embedded in text, improving domain adaptation by leveraging semantic consistency. To extract class-specific pixel features \mathbf{f}^c , we use the downsampled (same as feature shape) ground-truth mask to generate a binary mask b^c for class c and apply spatial averaging:

$$\mathbf{f}^c = \frac{1}{H} \cdot \frac{1}{W} \sum_{i=1}^H \sum_{j=1}^W b_{i,j}^c \cdot \mathbf{F}_{\text{sem},i,j} \quad (6)$$

where, $b^c \in \{0, 1\}$ indicates whether a pixel belongs to class c , and $\mathbf{F}_{\text{sem},i,j}$ is the pixel feature at location (i, j) . We then construct covariance matrices for pixel features Σ_p and the corresponding domain-agnostic text embeddings Σ_t :

$$\Sigma_p = [\text{Cov}(\mathbf{f}^i, \mathbf{f}^j)]_{i,j=1}^C, \Sigma_t = [\text{Cov}(\mathbf{t}^i, \mathbf{t}^j)]_{i,j=1}^C \quad (7)$$

where, \mathbf{f}^i and \mathbf{t}^i denote the feature vectors for class i , and C is the total number of classes. Due to typically small batch sizes

and the fact that not all classes are present in each mini-batch, we compute Σ_t using only the text embeddings corresponding to classes present in the sample. To address high variance in class pixel features, we use a memory bank $\mathbf{f}_{\text{current}}^c$ to store running averages, updated using an exponential decay:

$$\mathbf{f}_{\text{new}}^c = \lambda \cdot \mathbf{f}_{\text{current}}^c + (1 - \lambda) \cdot \mathbf{f}^c \quad (8)$$

The updated features $\mathbf{f}_{\text{new}}^c$ are used to compute Σ_p during training. The final VLCoL minimizes the cosine distance between the pixel covariance matrix Σ_p and the text covariance matrix Σ_t , encouraging the encoder’s feature space to emulate the semantic structure of the domain-agnostic text space:

$$\mathcal{L}_{\text{VLCoL}} = 1 - \frac{\langle \Sigma_p, \Sigma_t \rangle}{\|\Sigma_p\|_F \cdot \|\Sigma_t\|_F} \quad (9)$$

where $\langle \cdot, \cdot \rangle$ denotes the Frobenius inner product and $\|\cdot\|_F$ is the Frobenius norm. VLCoL can be seamlessly integrated into any UDA framework utilizing source-domain labels and unlabeled target-domain images. It effectively aligns the segmentation encoder’s latent space with the semantic relationships in the text embedding space.

D. Adversarial Learning for Structural Alignment

Following prior work [15], we enforce alignment of structural entropy distributions by training a discriminator to distinguish between domain-specific entropy maps. Specifically, for a batch of N labeled source samples $\{(I_n^{\text{src}}, Y_n^{\text{src}})\}_{n=1}^N$ and N unlabeled target images $\{I_n^{\text{tgt}}\}_{n=1}^N$, our segmentation network G generates pixel-wise probability maps P_n^{src} and P_n^{tgt} via the softmax function. We convert these probability maps into entropy maps E_n^{src} and E_n^{tgt} by computing the self-information at each pixel, i.e. the negative product of the probability and its logarithm. These entropy maps are then fed into a discriminator D , which is trained using a binary cross-entropy loss:

$$\mathcal{L}_D = \sum_{n=1}^N (\mathcal{L}_{\text{BCE}}(D(E_n^{\text{src}}), 1) + \mathcal{L}_{\text{BCE}}(D(E_n^{\text{tgt}}), 0)) \quad (10)$$

Meanwhile, the segmentation network (generator) is adversarially trained to fool the discriminator by minimizing:

$$\mathcal{L}_{\text{adv}} = \sum_{n=1}^N \mathcal{L}_{\text{BCE}}(D(E_n^{\text{tgt}}), 1) \quad (11)$$

This adversarial mechanism encourages the network to produce structurally consistent predictions across domains, effectively reducing entropy discrepancy and improving generalization on the target domain.

E. Prototype Alignment

From high-level feature \mathbf{F}_{high} extracted from the penultimate layer of the network, we collect pixel-level embeddings \mathbf{e}_v^s and \mathbf{e}_v^t , where v denotes a pixel, and the superscripts s and t refer to the source and target domains, respectively. For every class $c \in \{1, 2, \dots, C\}$, we compute class-specific prototypes from both domains. The source domain prototype \mathbf{z}_c^s is obtained

by averaging the feature vectors \mathbf{e}_v^s over all pixels that are labeled with class c , using the ground-truth label y_v^s . In the target domain, the prototype \mathbf{z}_c^t is calculated similarly, but using pseudo-labels \hat{y}_v^t , which are derived by taking the class with the maximum predicted softmax probability, i.e. $\hat{y}_v^t = \arg \max(\mathbf{p}_v^t)$. The set of pixels belonging to class c in the source and target domains are denoted by Ω_c^s and Ω_c^t , respectively. Inspired by [27], due to limited class representation in mini-batches during stochastic gradient descent (SGD) optimization, we maintain global prototypes updated with exponential moving averages rather than relying only on batch-level prototypes. This helps stabilize the semantic alignment over the course of training. The global prototype updates are performed as follows:

$$\mathbf{z}_c^s \leftarrow \beta \mathbf{z}_c^s + (1 - \beta) \cdot \frac{1}{|\Omega_c^s|} \sum_{v \in \Omega_c^s} \delta(y_v^s = c) \cdot \mathbf{e}_v^s \quad (12)$$

$$\mathbf{z}_c^t \leftarrow \beta \mathbf{z}_c^t + (1 - \beta) \cdot \frac{1}{|\Omega_c^t|} \sum_{v \in \Omega_c^t} \delta(\hat{y}_v^t = c) \cdot \mathbf{e}_v^t \quad (13)$$

where, $\beta \in [0, 1]$ is a momentum parameter that controls the influence of the current batch on the running prototype, and $\delta(\cdot)$ is the indicator function that equals 1 when the condition inside is true, and 0 otherwise. Finally, to enforce the alignment between source and target semantic spaces, we apply a prototype alignment loss. This loss penalizes the distance between corresponding source and target prototypes for each class using the squared ℓ_2 -norm:

$$\mathcal{L}_{\text{proto}} = \sum_{c=1}^C \|\mathbf{z}_c^s - \mathbf{z}_c^t\|^2 \quad (14)$$

By minimizing $\mathcal{L}_{\text{proto}}$, the model is encouraged to bring class-level feature representations from both domains closer together, thereby promoting better cross-domain semantic consistency and improving the segmentation performance under domain shift.

In summary, the overall training objective of the proposed segmentation network is defined as:

$$\mathcal{L}_{\text{total}} = \mathcal{L}_{\text{seg}} + \lambda_1 \mathcal{L}_{\text{adv}} + \lambda_2 \mathcal{L}_{\text{VLCOL}} + \lambda_3 \mathcal{L}_{\text{proto}} \quad (15)$$

where λ_1 , λ_2 and λ_3 are balance coefficients. The segmentation loss \mathcal{L}_{seg} is computed only on the labeled source images and defined in Eq. 5. \mathcal{L}_{adv} is the adversarial loss for domain alignment, defined in Eq. 11.

IV. EXPERIMENTS AND RESULTS

A. Datasets

1) *Cardiac Substructure Segmentation Dataset*: To evaluate the effectiveness of our proposed method, we conduct experiments on the Multi-Modality Whole Heart Segmentation (MMWHS) Challenge 2017 dataset [28], a widely used benchmark for cross-modality medical image segmentation. The dataset consists of 20 unpaired cardiac CT volumes and 20 unpaired cardiac MRI volumes, each with ground-truth annotations. These scans are collected from different imaging centers and patient cohorts, introducing significant domain shifts. We focus on segmenting four key cardiac structures:

the ascending aorta (AA), left atrium cavity (LAC), left ventricle cavity (LVC), and myocardium of the left ventricle (MYO). Domain adaptation is evaluated in both CT→MRI and MRI→CT directions.

2) *Abdominal Organ Segmentation Dataset*: We further validate our approach on an abdominal dataset consisting of 30 CT volumes from publicly available source [29] and 20 T2-SPIR MRI volumes from the ISBI 2019 CHAOS Challenge dataset [30]. Both modalities include pixel-wise annotations for four abdominal organs: Spleen, Right Kidney (RK), Left Kidney (LK), and Liver. We employ the preprocessed dataset provided by SIFA V2 [8].

3) *Brain Tumor Segmentation Dataset*: We also utilized the Multi-Modality Brain Tumor Segmentation Challenge 2018 (BraTS 2018) dataset [31] for tumor segmentation. This dataset comprises scans from 285 patients, including 210 high-grade glioma (HGG) and 75 low-grade glioma (LGG) cases, with four MRI modalities: T1, T1CE, T2, and FLAIR. For our experiments, we perform bidirectional domain adaptation between FLAIR and T2 modalities using the LGG subset.

For all datasets, we adopt an 80/20 training/testing split. The MMWHS dataset follows the same partition protocol as used in SIFA V2 [8], while the abdominal and brain datasets are partitioned based on fixed random seeds (value 42) for reproducibility. The partition of data are based on a subject level to ensure non-overlapping training and testing sets. During training, 2D image slices are randomly selected from the training subjects and fed into the networks. Segmentation performance is assessed using Dice Similarity Coefficient (Dice) and Average Symmetric Surface Distance (ASD), where higher Dice and lower ASD values indicate better segmentation quality.

B. Implementation Details

We implement our framework using DeepLabV2 [35] as the backbone segmentation network G , initialized with ImageNet-pretrained weights [36]. For adversarial training, we employ a PatchGAN [37] style discriminator D , composed of four convolutional layers followed by a classification layer. All input images are resized to 256×256 pixels, and standard augmentation techniques—random scaling, rotation, and intensity variation—are applied to improve generalization. The segmentation model is trained using SGD with a learning rate of 2.5×10^{-4} , momentum 0.9, and weight decay 5×10^{-4} , following optimization strategies from [6], [14]. The discriminator and text fusion module are trained using Adam with a learning rate of 1×10^{-4} . We use a batch size of 4 and set key hyperparameters as follows: temperature $\tau = 0.05$, balance factor $\alpha = 0.2$, adversarial weight $\lambda_{\text{adv}} = 0.003$, and feature alignment weight $\lambda_{\text{epc}} = 0.1/0.01$ for CT→MRI and MRI→CT (similarly for FLAIR→T2 and T2→FLAIR), respectively. The prototype update coefficient is $\beta = 0.01$, and the weights for various loss components are $\lambda_1 = 0.003$, $\lambda_2 = 1.0$, and $\lambda_3 = 0.1$. All models are implemented in PyTorch and trained on a single NVIDIA A100 GPU with 40 GB memory. For a more robust evaluation, each experiment was conducted with different model initializations, and the average values were used for analysis.

TABLE I
COMPARISON OF SEGMENTATION PERFORMANCE ON THE MMWHS DATASET FOR CARDIAC MRI \rightarrow CT AND CT \rightarrow MRI DOMAIN ADAPTATION.

Method	MRI \rightarrow CT										CT \rightarrow MRI									
	Dice (\uparrow)					ASD (\downarrow)					Dice (\uparrow)					ASD (\downarrow)				
	AA	LAC	LVC	MYO	Avg	AA	LAC	LVC	MYO	Avg	AA	LAC	LVC	MYO	Avg	AA	LAC	LVC	MYO	Avg
Supervised training	89.3	91.4	92.8	88.0	90.4	2.3	2.9	1.5	3.2	2.5	81.6	86.3	92.3	80.0	85.1	3.4	2.1	1.7	1.6	2.2
W/o adaptation	30.8	36.8	18.3	7.2	23.3	20.2	8.9	33.6	27.8	22.6	18.5	7.3	53.5	2.1	20.4	7.1	25.8	8.7	29.9	17.9
CycleGAN [5]	73.8	75.7	52.3	28.7	57.6	11.5	13.6	9.2	8.6	10.8	64.3	30.7	65.0	43.0	50.7	5.8	9.8	6.0	5.0	6.6
AdaOutput [14]	73.5	80.4	76.1	48.6	69.6	15.5	5.8	5.2	6.6	8.3	52.3	71.1	79.5	49.2	63.2	9.0	3.5	5.1	5.4	5.8
PnP-AdaNet [32]	74.0	68.9	61.9	50.8	63.9	12.8	6.3	17.4	14.7	12.8	43.7	47.0	77.7	48.6	54.3	11.4	14.5	4.5	5.3	8.9
AdvEnt [15]	79.5	83.0	79.5	57.7	75.0	13.9	9.3	6.9	4.5	8.7	52.3	71.1	79.5	49.2	63.2	9.0	3.5	5.1	5.4	5.8
SIFA V2 [8]	81.3	79.5	73.8	61.6	74.1	7.9	6.2	5.5	8.5	7.0	65.3	62.3	78.9	47.3	63.4	7.3	7.4	3.8	4.4	5.7
EBM [33]	78.9	80.7	75.7	60.4	74.9	8.6	6.4	4.7	8.2	7.1	65.9	64.2	76.9	49.1	64.0	6.9	7.5	5.6	3.8	6.0
CRST [34]	79.6	80.5	78.3	63.7	75.5	8.8	6.4	4.5	7.5	6.8	65.1	66.9	77.2	50.0	64.8	6.4	6.3	5.5	4.0	5.6
DAFormer [17]	85.5	88.2	74.5	60.2	77.1	12.1	9.2	7.7	4.9	8.5	75.2	59.4	72.0	57.1	65.9	4.7	13.8	11.6	7.8	9.5
ADR [10]	87.9	86.8	82.1	64.2	80.2	5.9	4.1	4.8	5.7	5.1	66.9	69.1	81.0	48.3	66.3	6.9	5.5	3.4	4.0	4.9
SECASA [6]	83.8	85.2	82.9	71.7	80.9	9.6	4.2	3.9	3.9	5.4	68.3	74.6	81.0	55.9	69.9	4.9	3.6	5.4	3.2	4.3
MA-UDA [18]	90.8	88.7	77.6	67.4	81.1	5.7	3.8	7.6	5.2	5.6	71.0	67.4	77.5	59.1	68.7	4.4	6.9	5.6	4.2	5.3
Ours	82.5	87.1	85.7	74.3	82.4	13.2	7.2	3.5	3.6	6.9	69.0	74.9	83.5	59.2	71.6	5.3	4.5	5.7	5.0	5.1

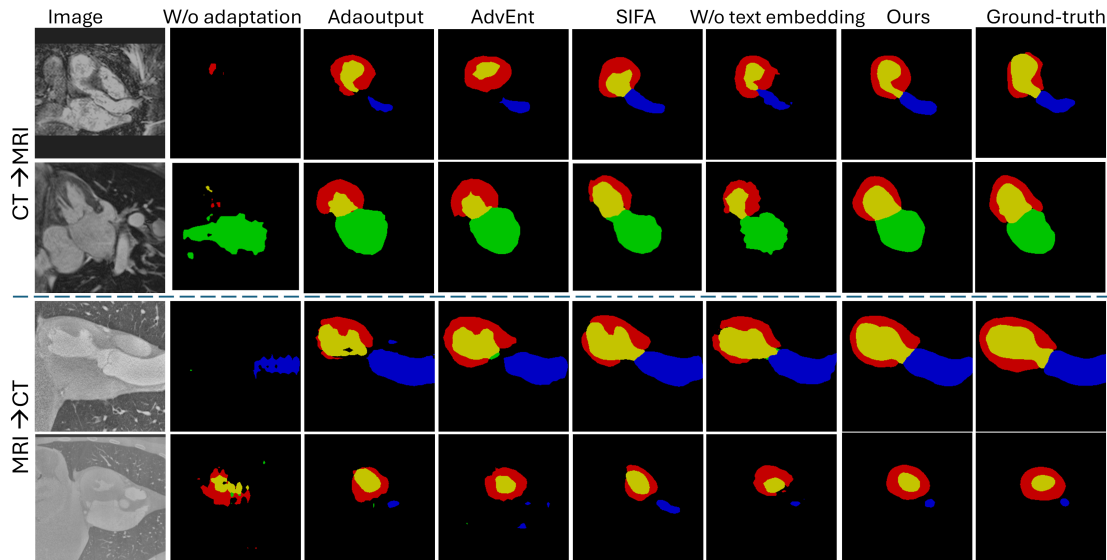


Fig. 3. Qualitative segmentation results by different comparison algorithms. The blue, green, yellow and red represent the AA, LAC, LVC and MYO, respectively

C. Comparison with Existing UDAs

We evaluated the performance of our TCSA-UDA against existing domain adaptation methods, including image-level, feature-level, output-level, transformer-based, and semantic-aware approaches, as detailed in Table I. For fairness and consistency, we adopted the reported experimental settings from the original works wherever available. Methods lacking public implementations were either re-implemented using the same configuration as SIFA [8] or their published results were cited directly for comparison.

1) *Results from Cardiac Substructure Segmentation:* For the MRI \rightarrow CT transfer task, Table I shows that the baseline model without adaptation performs poorly, achieving an average Dice score of only 23.3, while the upper-bound supervised

training yields 90.4. Image-level methods like CycleGAN and SIFA V2 focus on style translation but suffer from semantic inconsistency. Our method notably improves CT \rightarrow MRI Dice (50.7 to 71.6) and MRI \rightarrow CT Dice (57.6 to 82.4), with better ASD values, demonstrating stronger anatomical fidelity. Feature-level methods such as CRST, EBM and ADR align latent spaces, yet fall short in structure precision. Our Dice scores exceed CRST and EBM in both directions for example, MRI \rightarrow CT Dice improves from 74.9 (EBM) to 82.4, while maintaining lower ASD (6.9 vs. 7.1). Output-level methods, including AdvEnt and AdaOutput, act on prediction maps but lack structural constraints. Our Dice (CT \rightarrow MRI: 71.6 vs. AdaOutput’s 63.2) and ASD (5.1 vs. 5.8) reflect stronger regularization via combined semantic and feature guidance.

TABLE II
COMPARISON OF ABDOMINAL ORGAN SEGMENTATION PERFORMANCE FROM ABDOMINAL MRI \rightarrow CT

Method	Dice (\uparrow)					ASD (\downarrow)				
	Spleen	RK	LK	Liver	Avg	Spleen	RK	LK	Liver	Avg
Supervised	84.83 \pm 0.60	89.95 \pm 1.43	88.32 \pm 2.06	91.44 \pm 1.30	88.64 \pm 1.13	0.90 \pm 0.06	0.47 \pm 0.06	0.59 \pm 0.10	0.22 \pm 0.10	0.54 \pm 0.04
AdaOutput [14]	77.41 \pm 0.73	77.27 \pm 0.54	74.30 \pm 0.81	85.33 \pm 0.56	78.57 \pm 0.54	0.94 \pm 0.18	1.23 \pm 0.40	1.65 \pm 0.13	0.86 \pm 0.06	1.17 \pm 0.14
AdvEnt [15]	76.82 \pm 1.21	77.22 \pm 0.57	74.67 \pm 1.00	85.25 \pm 0.62	78.50 \pm 0.61	1.03 \pm 0.17	1.11 \pm 0.18	1.71 \pm 0.12	0.87 \pm 0.05	1.18 \pm 0.08
SIFA [8]	78.75 \pm 0.81	80.92 \pm 0.52	78.58 \pm 0.58	87.84 \pm 0.19	81.52 \pm 0.35	1.30 \pm 0.07	0.74 \pm 0.06	1.14 \pm 0.12	0.57 \pm 0.06	0.94 \pm 0.04
SECASA [6]	75.52 \pm 0.35	77.07 \pm 0.74	73.95 \pm 0.34	85.93 \pm 0.77	78.62 \pm 0.27	1.51 \pm 0.29	1.09 \pm 0.14	1.69 \pm 0.13	0.82 \pm 0.15	1.27 \pm 0.06
Ours	81.15 \pm 0.49	83.72 \pm 0.40	80.35 \pm 0.11	88.43 \pm 0.39	83.41 \pm 0.30	0.88 \pm 0.12	0.64 \pm 0.06	0.79 \pm 0.08	0.52 \pm 0.08	0.71 \pm 0.07

TABLE III
COMPARISON OF ABDOMINAL ORGAN SEGMENTATION PERFORMANCE FROM ABDOMINAL CT \rightarrow MRI

Method	Dice (\uparrow)					ASD (\downarrow)				
	Spleen	RK	LK	Liver	Avg	Spleen	RK	LK	Liver	Avg
Supervised	85.60 \pm 1.76	87.79 \pm 0.97	87.22 \pm 0.70	91.06 \pm 1.35	87.92 \pm 0.65	1.42 \pm 0.13	0.25 \pm 0.07	1.70 \pm 0.15	0.31 \pm 0.02	0.92 \pm 0.07
AdaOutput [14]	58.25 \pm 1.06	79.42 \pm 0.76	68.53 \pm 0.95	89.55 \pm 0.52	73.94 \pm 0.61	2.62 \pm 0.34	0.90 \pm 0.13	1.77 \pm 0.22	0.54 \pm 0.11	1.46 \pm 0.14
AdvEnt [15]	57.62 \pm 1.12	82.40 \pm 0.39	68.55 \pm 0.42	89.57 \pm 0.30	74.54 \pm 0.37	2.68 \pm 0.18	0.65 \pm 0.04	1.92 \pm 0.15	0.50 \pm 0.08	1.44 \pm 0.09
SIFA [8]	71.67 \pm 0.52	87.77 \pm 0.51	75.57 \pm 0.40	90.48 \pm 0.26	81.37 \pm 0.25	1.75 \pm 0.09	0.42 \pm 0.05	1.69 \pm 0.13	0.39 \pm 0.08	1.06 \pm 0.07
SECASA [6]	69.70 \pm 1.22	82.55 \pm 1.32	73.17 \pm 0.36	89.95 \pm 0.13	78.84 \pm 0.64	2.43 \pm 0.58	0.68 \pm 0.06	1.87 \pm 0.22	0.53 \pm 0.12	1.38 \pm 0.22
Ours	77.30 \pm 0.49	89.32 \pm 0.55	75.52 \pm 0.44	90.31 \pm 0.42	83.11 \pm 0.29	1.72 \pm 0.12	0.40 \pm 0.08	1.71 \pm 0.08	0.41 \pm 0.07	1.06 \pm 0.06

Transformer-based models, such as DAFormer and MA-UDA, leverage global semantics. MA-UDA adds meta-adaptation to dynamically tune representations for each domain. Our method achieves higher CT \rightarrow MRI Dice (71.6 vs. MA-UDA’s 69.4) and MRI \rightarrow CT Dice (82.4 vs. DAFormer’s 77.1), highlighting superior cross-domain generalization. Lastly, semantic-aware methods integrate class-level cues; SECASA is competitive with 80.9 Dice (MRI \rightarrow CT), but our model surpasses this (82.4) while holding steady on ASD. CT \rightarrow MRI Dice (71.6 vs. 69.9 in SECASA) also favors our method, showing that semantic representation is enhanced without sacrificing boundary precision. Our method significantly reduces domain shift compared to the non-adapted baseline, closing 88.1% of the Dice gap for MRI \rightarrow CT adaptation and 79.1% for CT \rightarrow MRI. Statistical significance testing ($p < 0.01$) was performed between our method and implemented state-of-the-art approaches, confirming the reliability of its improvements across both MRI \rightarrow CT and CT \rightarrow MRI tasks. Figure 3 showcases slice images to illustrate the effectiveness of our method in cardiac structure segmentation across CT and MRI domains. Our approach delivers more accurate and consistent results compared to baseline and UDA methods. By effectively addressing domain shift and preserving both edge sharpness and foreground integrity, the segmented structures closely match the ground truth in both MRI \rightarrow CT and CT \rightarrow MRI directions. These consistent improvements across both transfer directions validate the robustness of our approach in handling domain shifts, delivering enhanced segmentation accuracy and spatial coherence for cross-modality cardiac image analysis.

2) *Results from Abdominal Organ Segmentation:* Table II and Table III show the comparative performance of abdominal organ segmentation, where the supervised model serves as the upper bound and our proposed TCSA-USD achieves significant improvements over existing unsupervised domain adaptation methods. For MRI \rightarrow CT, TCSA-USD attains an average Dice of 83.41% and ASD of 0.71 mm, outperforming SIFA and SECASA. For CT \rightarrow MRI, it achieves 83.11% Dice and 1.06 mm ASD, again surpassing competing approaches.

These consistent gains highlight TCSA-USD’s effectiveness in bridging domain gaps and enhancing cross-modality segmentation accuracy through to different anatomical structures and imaging modalities. Additionally, our experiments that segmentation methods perform significantly better on abdominal organs than cardiac structures due to anatomical and imaging differences. Abdominal organs are spatially distinct, easing boundary detection, while cardiac structures are closely intertwined, complicating segmentation. Moreover, by leveraging semantic information from textual descriptions of organ classes, the model gains a richer understanding of each structure’s contextual and anatomical characteristics. Fig. 4 highlights our method’s effectiveness in abdominal segmentation under bidirectional domain adaptation, producing anatomically plausible and semantically consistent results. Notably, it achieves superior boundary delineation, especially for the liver and spleen, demonstrating robustness in capturing structural and contextual cues where organ separation is clear and modality differences are moderate.

TABLE IV
COMPARATIVE RESULTS OF BIDIRECTIONAL ADAPTATION FOR BRAIN TUMOR SEGMENTATION ON BRATS

Method	FLAIR \rightarrow T2		T2 \rightarrow FLAIR	
	Dice (\uparrow)	ASD (\downarrow)	Dice (\uparrow)	ASD (\downarrow)
Supervised	80.72 \pm 1.42	5.10 \pm 0.71	75.16 \pm 1.56	5.06 \pm 1.13
AdaOutput [14]	67.56 \pm 1.21	6.63 \pm 1.05	67.73 \pm 1.71	5.36 \pm 1.71
AdvEnt [15]	67.32 \pm 1.32	6.74 \pm 1.16	65.84 \pm 2.56	5.83 \pm 1.94
SIFA [8]	71.50 \pm 0.95	6.62 \pm 0.42	72.71 \pm 1.46	5.67 \pm 1.23
SECASA [6]	68.27 \pm 1.08	6.92 \pm 1.20	70.97 \pm 1.51	5.64 \pm 1.83
Ours	73.08 \pm 0.92	7.20 \pm 0.26	73.58 \pm 0.61	5.90 \pm 1.07

3) *Results from Brain Tumor Segmentation:* Table IV presents quantitative results for bidirectional brain tumor segmentation across FLAIR \rightarrow T2 and T2 \rightarrow FLAIR adaptations. For FLAIR \rightarrow T2, our method achieves a Dice score of 73.08 \pm 0.92, outperforming unsupervised baselines such as AdaOutput (67.56 \pm 1.21), AdvEnt (67.32 \pm 1.32), SECASA (68.27 \pm 1.08), and SIFA (71.50 \pm 0.95), with a competitive

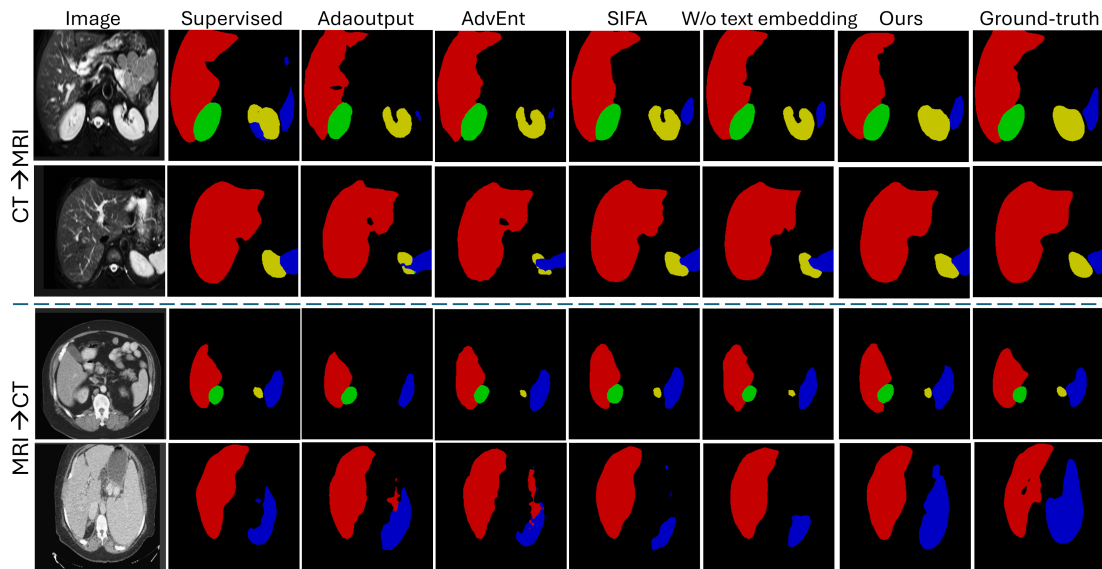


Fig. 4. Qualitative results of Abdominal organ segmentation by different comparison algorithms. The blue, green, yellow and red represent the Spleen, RK, LK and Liver, respectively

ASD of 7.20 ± 0.26 . For $T2 \rightarrow FLAIR$, we achieve 73.58 ± 0.61 Dice and 5.90 ± 1.07 ASD, surpassing other unsupervised methods. Fig. 5 presents the qualitative outcomes of our approach. Notably, the segmentation map produced by our method demonstrates superior preservation of the tumor’s shape and boundary.

D. Ablation Study

Table V presents an ablation study evaluating the contribution of key components and their corresponding loss functions on the $MRI \rightarrow CT$ domain adaptation task. The baseline setup includes the segmentation loss (L_{seg}) and adversarial loss (L_{adv}), achieving an average Dice score of 74.7%. Incorporating the prototype alignment loss (L_{proto}) improves performance to 77.1%, indicating that semantic alignment between domains enhances segmentation. Including baseline with the proposed visual-language covariance cosine loss (L_{VLCoL}) yields a significant boost to 81.2%, demonstrating its stronger capacity to guide domain adaptation by leveraging visual-language consistency. When both L_{proto} and L_{VLCoL} are jointly applied alongside L_{seg} and L_{adv} , the model achieves the best performance with an average Dice score of 82.4%. These results highlight the complementary nature of prototype-based alignment and visual-language covariance learning, and confirm that their integration leads to more robust cross-domain feature learning and improved segmentation accuracy.

To evaluate the effectiveness of our proposed modality-aware vision-language fusion approach, we conducted a comprehensive ablation study focusing on two key factors: (1) the impact of different text embedding methods and prompt templates, and (2) the role of transformer-based fusion in aligning vision and language representations. As shown in Table VI, models utilizing textual embeddings consistently outperformed the vision-only baseline, highlighting the benefit of incorporating

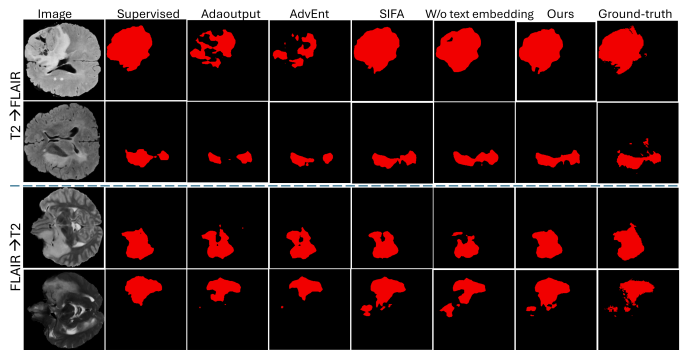


Fig. 5. Qualitative results of brain tumor segmentation by different comparison algorithms

TABLE V
ABLATION STUDY OF KEY COMPONENTS AND THEIR LOSS OPTIMIZATION ON THE ADAPTATION TASK FOR $MRI \rightarrow CT$. P-VALUE ARE COMPUTED RELATIVE TO THE BASELINE.

Method	L_{seg}	L_{adv}	L_{proto}	L_{VLCoL}	Avg Dice	p-value
Baseline	✓	✓			74.7	-
+ PA only	✓	✓	✓		77.1	p<0.0001
+ Text-driven only	✓	✓		✓	81.2	p<0.0001
Ours	✓	✓	✓	✓	82.4	p<0.0001

TABLE VI
ABLATION STUDY OF DIFFERENT EMBEDDING METHODS WITH THEIR PROMPT TEMPLATES FOR CARDIAC $MRI \rightarrow CT$ AND $CT \rightarrow MRI$ ADAPTATION TASK

Embedding method	Prompt template	Avg. Dice↑ (MRI → CT)	Avg. Dice↑ (CT → MRI)
Vision-Only	-	74.7	64.5
BioBERT	A CT/MRI imaging of a [CLS].	81.3	69.9
CLIP	A photo of [CLS].	78.5	68.3
CLIP	There is [CLS] in this cardiac CT/MRI.	79.9	69.1
CLIP (Ours)	A cardiac CT/MRI imaging of a [CLS].	82.4	71.6

semantic priors from language. Among various embeddings, our CLIP-based modality-specific prompt, "A cardiac CT/MRI imaging of a [CLS]", achieved the best performance, with 82.4% and 71.6% average Dice scores for MRI→CT and CT→MRI adaptation, respectively. These results demonstrate that carefully crafted, modality-specific prompts provide more contextually relevant semantic guidance, leading to better domain adaptation. Further analysis in Table VII emphasizes the

TABLE VII
ABLATION EXPERIMENT RESULTS FOR THE COMBINATION OF
MODALITY-SPECIFIC PROMPT AND TRANSFORMER FUSION

Method	Avg. Dice↑ (MRI → CT)	Avg. Dice↑ (CT → MRI)
Shared prompt + w/o transformer fusion	77.6	65.6
Shared prompt + with transformer fusion	78.5	68.3
Modality-specific prompt + w/o transformer fusion	77.6	65.7
Modality-specific prompt + with transformer fusion	82.4	71.6

complementary role of transformer-based fusion. While shared prompts with fusion improved performance over the non-fused version, combining modality-specific text prompts with transformer fusion yielded the highest gains, outperforming all other configurations. Notably, 'w/o transformer fusion' refers to configurations that exclude MHA and MLP layers from the architecture. The shared text prompt used for all shared configurations is 'A photo of [CLS].'

E. GradCAM Visualization Analysis

The GradCAM visualizations in Figure 6 provide a detailed view of how attention regions evolve with progressive loss optimization in the TCSA-UDA (Text-Driven Cross-Semantic Alignment for Unsupervised Domain Adaptation) framework. Initially, with the basic combination of segmentation and adversarial losses ($\mathcal{L}_{seg} + \mathcal{L}_{adv}$), the attention maps are broad and loosely aligned with semantic regions, indicating limited semantic precision despite domain alignment. The introduction of the prototype loss (\mathcal{L}_{proto}) enhances class-wise feature consistency, resulting in more focused and semantically meaningful attention. The most significant refinement is observed with the inclusion of the vision-language covariance cosine loss (\mathcal{L}_{VLCOL}), which leverages cross-modal covariance to guide the model's attention toward contextually relevant and semantically rich regions. This loss encourages alignment between visual features and textual semantics, leading to highly localized and accurate attention maps that closely match ground-truth segmentation. Block-wise, the attention transitions from general domain-level features to fine-grained semantic regions, demonstrating the cumulative impact of each loss component. The final configuration, integrating all loss terms, highlights the synergy between visual and textual modalities, enabling robust cross-domain generalization and precise semantic alignment. These visualizations validate the effectiveness of TCSA-UDA in enhancing attention and segmentation performance through text-driven semantic guidance.

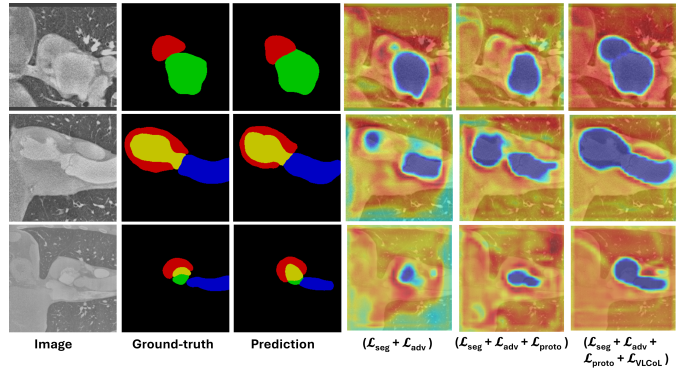


Fig. 6. GradCAM visualization results comparing attention regions across different loss configurations in the TCSA-UDA framework. From left to right: input image, ground-truth segmentation, predicted segmentation, and GradCAM maps for models trained with progressively enhanced loss functions— $\mathcal{L}_{seg} + \mathcal{L}_{adv}$, $\mathcal{L}_{seg} + \mathcal{L}_{adv} + \mathcal{L}_{proto}$, and $\mathcal{L}_{seg} + \mathcal{L}_{adv} + \mathcal{L}_{proto} + \mathcal{L}_{VLCOL}$.

V. CONCLUSION

This paper presents TCSA-UDA, a novel unsupervised domain adaptation framework for medical image segmentation that integrates modality-aware text embeddings with visual features to guide semantic alignment through covariance learning and adversarial training. Unlike conventional methods, TCSA-UDA leverages modality-specific class-level textual semantics to facilitate robust modality-agnostic representation learning, enabling effective knowledge transfer between CT and MRI without requiring target domain annotations. The proposed approach aligns visual and textual modalities in a shared feature space, enhancing semantic consistency across domains. Evaluations on challenging cross-modality cardiac (MRI→CT and CT→MRI), abdominal, and brain tumor segmentation tasks demonstrate that TCSA-UDA consistently outperforms existing UDA methods. Notably, it excels in segmenting anatomically challenging structures such as the left ventricle cavity (LVC) and myocardium (MYO) as well as complex regions in abdominal and irregular tumor boundaries. These results validate the effectiveness of leveraging textual guidance for semantic alignment and highlight the potential of TCSA-UDA in addressing domain shifts in medical image segmentation. In future work, we plan to incorporate LLM-based long-form domain descriptors to generate more representative and domain-agnostic embeddings, bringing averaged embeddings closer to domain centroids in latent space and enhancing cross-domain generalization.

REFERENCES

- [1] M. C. Florkow, K. Willemsen, V. V. Mascarenhas, E. H. Oei, M. van Stralen, and P. R. Seevinck, "Magnetic resonance imaging versus computed tomography for three-dimensional bone imaging of musculoskeletal pathologies: a review," *Journal of Magnetic Resonance Imaging*, vol. 56, no. 1, pp. 11–34, 2022.
- [2] S. Deng, Y. Chen, W. Huang, R. Zhang, and Z. Xiong, "Unsupervised domain adaptation for em image denoising with invertible networks," *IEEE Transactions on Medical Imaging*, vol. 44, no. 1, pp. 92–105, 2025.
- [3] C. Chen, Q. Dou, H. Chen, J. Qin, and P.-A. Heng, "Synergistic image and feature adaptation: Towards cross-modality domain adaptation for medical image segmentation," in *Proceedings of the AAAI Conference on Artificial Intelligence*, vol. 33, pp. 865–872, 2019.

- [4] X. Liu, C. Yoo, F. Xing, H. Oh, G. El Fakhri, J.-W. Kang, J. Woo, *et al.*, “Deep unsupervised domain adaptation: A review of recent advances and perspectives,” *APSIPA Transactions on Signal and Information Processing*, vol. 11, no. 1, 2022.
- [5] J.-Y. Zhu, T. Park, P. Isola, and A. A. Efros, “Unpaired image-to-image translation using cycle-consistent adversarial networks,” in *IEEE International Conference on Computer Vision (ICCV)*, pp. 2242–2251, 2017.
- [6] W. Feng, L. Ju, L. Wang, K. Song, X. Zhao, and Z. Ge, “Unsupervised domain adaptation for medical image segmentation by selective entropy constraints and adaptive semantic alignment,” *Proceedings of the AAAI Conference on Artificial Intelligence*, vol. 37, pp. 623–631, Jun. 2023.
- [7] M. Long, Y. Cao, J. Wang, and M. Jordan, “Learning transferable features with deep adaptation networks,” in *International Conference on Machine Learning*, pp. 97–105, PMLR, 2015.
- [8] C. Chen, Q. Dou, H. Chen, J. Qin, and P. A. Heng, “Unsupervised bidirectional cross-modality adaptation via deeply synergistic image and feature alignment for medical image segmentation,” *IEEE Transactions on Medical Imaging*, vol. 39, no. 7, pp. 2494–2505, 2020.
- [9] Z. Zhao, F. Zhou, K. Xu, Z. Zeng, C. Guan, and S. K. Zhou, “L-uda: Label-efficient unsupervised domain adaptation for medical image segmentation,” *IEEE Transactions on Medical Imaging*, vol. 42, no. 3, pp. 633–646, 2022.
- [10] X. Sun, Z. Liu, S. Zheng, C. Lin, Z. Zhu, and Y. Zhao, “Attention-enhanced disentangled representation learning for unsupervised domain adaptation in cardiac segmentation,” in *International Conference on Medical Image Computing and Computer-Assisted Intervention*, pp. 745–754, Springer, 2022.
- [11] Y. Zou, Z. Yu, B. V. Kumar, and J. Wang, “Unsupervised domain adaptation for semantic segmentation via class-balanced self-training,” in *Proceedings of the European Conference on Computer Vision (ECCV)*, September 2018.
- [12] Y. Li, L. Yuan, and N. Vasconcelos, “Bidirectional learning for domain adaptation of semantic segmentation,” in *Proceedings of the IEEE/CVF Conference on Computer Vision and Pattern Recognition (CVPR)*, June 2019.
- [13] Y. Zhang, Y. Wei, Q. Wu, P. Zhao, S. Niu, J. Huang, and M. Tan, “Collaborative unsupervised domain adaptation for medical image diagnosis,” *IEEE Transactions on Image Processing*, vol. 29, pp. 7834–7844, 2020.
- [14] Y.-H. Tsai, W.-C. Hung, S. Schuster, K. Sohn, M.-H. Yang, and M. Chandraker, “Learning to adapt structured output space for semantic segmentation,” in *IEEE Conference on Computer Vision and Pattern Recognition*, pp. 7472–7481, 2018.
- [15] T.-H. Vu, H. Jain, M. Bucher, M. Cord, and P. Pérez, “Advent: Adversarial entropy minimization for domain adaptation in semantic segmentation,” in *Proceedings of the IEEE/CVF Conference on Computer Vision and Pattern Recognition*, pp. 2517–2526, 2019.
- [16] Q. En and Y. Guo, “Unsupervised domain adaptation for medical image segmentation with dynamic prototype-based contrastive learning,” in *Conference on Health, Inference, and Learning*, pp. 312–325, PMLR, 2024.
- [17] L. Hoyer, D. Dai, and L. Van Gool, “Daformer: Improving network architectures and training strategies for domain-adaptive semantic segmentation,” in *IEEE/CVF Conference on Computer Vision and Pattern Recognition (CVPR)*, pp. 9914–9925, 2022.
- [18] W. Ji and A. C. S. Chung, “Unsupervised domain adaptation for medical image segmentation using transformer with meta attention,” *IEEE Transactions on Medical Imaging*, vol. 43, no. 2, pp. 820–831, 2024.
- [19] N. K. Tomar, D. Jha, U. Bagci, and S. Ali, “Tganet: Text-guided attention for improved polyp segmentation,” in *International Conference on Medical Image Computing and Computer-Assisted Intervention*, pp. 151–160, Springer, 2022.
- [20] Y. Zhong, M. Xu, K. Liang, K. Chen, and M. Wu, “Ariadne’s thread: Using text prompts to improve segmentation of infected areas from chest x-ray images,” in *International Conference on Medical Image Computing and Computer-Assisted Intervention*, pp. 724–733, Springer, 2023.
- [21] C. Liu, S. Cheng, C. Chen, M. Qiao, W. Zhang, A. Shah, W. Bai, and R. Arcucci, “M-flag: Medical vision-language pre-training with frozen language models and latent space geometry optimization,” in *International Conference on Medical Image Computing and Computer-Assisted Intervention*, pp. 637–647, Springer, 2023.
- [22] Y. Chen, C. Liu, W. Huang, S. Cheng, R. Arcucci, and Z. Xiong, “Generative text-guided 3d vision-language pretraining for unified medical image segmentation,” *arXiv preprint arXiv:2306.04811*, 2023.
- [23] Z. Liu, Z. Zhu, S. Zheng, Y. Liu, J. Zhou, and Y. Zhao, “Margin preserving self-paced contrastive learning towards domain adaptation for medical image segmentation,” *IEEE Journal of Biomedical and Health Informatics*, vol. 26, no. 2, pp. 638–647, 2022.
- [24] Z. Du, X. Li, F. Li, K. Lu, L. Zhu, and J. Li, “Domain-agnostic mutual prompting for unsupervised domain adaptation,” in *IEEE/CVF Conference on Computer Vision and Pattern Recognition (CVPR)*, pp. 23375–23384, June 2024.
- [25] A. Radford, J. W. Kim, C. Hallacy, A. Ramesh, G. Goh, S. Agarwal, G. Sastry, A. Askell, P. Mishkin, J. Clark, G. Krueger, and I. Sutskever, “Learning transferable visual models from natural language supervision,” in *Proceedings of the 38th International Conference on Machine Learning* (M. Meila and T. Zhang, eds.), vol. 139 of *Proceedings of Machine Learning Research*, pp. 8748–8763, PMLR, 18–24 Jul 2021.
- [26] J. Lee, W. Yoon, S. Kim, D. Kim, S. Kim, C. H. So, and J. Kang, “BioBERT: a pre-trained biomedical language representation model for biomedical text mining,” *Bioinformatics*, vol. 36, pp. 1234–1240, 09 2019.
- [27] S. Xie, Z. Zheng, L. Chen, and C. Chen, “Learning semantic representations for unsupervised domain adaptation,” in *International Conference on Machine Learning*, pp. 5423–5432, PMLR, 2018.
- [28] X. Zhuang and J. Shen, “Multi-scale patch and multi-modality atlases for whole heart segmentation of mri,” *Medical Image Analysis*, vol. 31, pp. 77–87, 2016.
- [29] B. Landman, Z. Xu, J. Igelsias, M. Styner, T. Langerak, and A. Klein, “Miccai multi-atlas labeling beyond the cranial vault—workshop and challenge,” in *Proc. MICCAI multi-atlas labeling beyond cranial vault—workshop challenge*, vol. 5, p. 12, Munich, Germany, 2015.
- [30] A. E. Kavur, N. S. Gezer, M. Barış, S. Aslan, P.-H. Conze, V. Groza, D. D. Pham, S. Chatterjee, P. Ernst, S. Özkan, *et al.*, “Chaos challenge-combined (ct-mr) healthy abdominal organ segmentation,” *Medical Image Analysis*, vol. 69, p. 101950, 2021.
- [31] B. H. Menze, A. Jakab, S. Bauer, J. Kalpathy-Cramer, K. Farahani, J. Kirby, Y. Burren, N. Porz, J. Slotboom, R. Wiest, *et al.*, “The multimodal brain tumor image segmentation benchmark (brats),” *IEEE Transactions on Medical Imaging*, vol. 34, no. 10, pp. 1993–2024, 2014.
- [32] Q. Dou, C. Ouyang, C. Chen, H. Chen, B. Glocker, X. Zhuang, and P.-A. Heng, “Pnp-adanet: Plug-and-play adversarial domain adaptation network at unpaired cross-modality cardiac segmentation,” *IEEE Access*, vol. 7, pp. 99065–99076, 2019.
- [33] X. Liu, B. Hu, X. Liu, J. Lu, J. You, and L. Kong, “Energy-constrained self-training for unsupervised domain adaptation,” in *25th International Conference on Pattern Recognition (ICPR)*, pp. 7515–7520, 2021.
- [34] Y. Zou, Z. Yu, X. Liu, B. V. K. V. Kumar, and J. Wang, “Confidence regularized self-training,” in *IEEE/CVF International Conference on Computer Vision (ICCV)*, pp. 5981–5990, 2019.
- [35] L.-C. Chen, G. Papandreou, I. Kokkinos, K. Murphy, and A. L. Yuille, “Deeplab: Semantic image segmentation with deep convolutional nets, atrous convolution, and fully connected crfs,” *IEEE Transactions on Pattern Analysis and Machine Intelligence*, vol. 40, no. 4, pp. 834–848, 2017.
- [36] J. Deng, W. Dong, R. Socher, L.-J. Li, K. Li, and L. Fei-Fei, “Imagenet: A large-scale hierarchical image database,” in *IEEE Conference on Computer Vision and Pattern Recognition*, pp. 248–255, Ieee, 2009.
- [37] P. Isola, J.-Y. Zhu, T. Zhou, and A. A. Efros, “Image-to-image translation with conditional adversarial networks,” in *IEEE Conference on Computer Vision and Pattern Recognition*, pp. 1125–1134, 2017.